Hu *et al. Energy Mater.* **2025**, *5*, 500078
DOI: 10.20517/energymater.2024.161

Energy Materials

Article

Open Access

Check for updates

Zwitterionic gemini additive as interface engineers for long-life aqueous Zn/TEMPO flow batteries with enhanced areal capacity

Feiyang Hu[1], Zhiwen Cui[2], Zhen Dong[3], Liyuan Jiang[4], Nwaji Njemuwa Njoku[5], Wenzhang Dong[1], Hao Fan[1,*], Mahalingam Ravivarma[1,*], Jianbao Wu[4], Duanyang Kong[2,*], Jiangxuan Song[1]

[1]State Key Laboratory for Mechanical Behavior of Materials, Shaanxi International Research Center for Soft Matter, School of Materials Science and Engineering, Xi'an Jiaotong University, Xi'an 710049, Shaanxi, China.
[2]State Key Laboratory of Chemical Resource Engineering, Beijing University of Chemical Technology, Beijing 100029, China.
[3]Shaanxi Coal Chemical Industry Technology Research Institute Co. Ltd., Xi'an 710100, Shaanxi, China.
[4]School of Mathematics, Physics and Statistics, Shanghai University of Engineering Science, Shanghai 201620, China.
[5]Institute of Fundamental Technological Research, Polish Academy of Sciences, Warsaw 02-106, Poland.

***Correspondence to:** Dr. Hao Fan, State Key Laboratory for Mechanical Behavior of Materials, Shaanxi International Research Center for Soft Matter, School of Materials Science and Engineering, Xi'an Jiaotong University, Xi'an 710049, Shaanxi, China. E-mail: fanh2018@xjtu.edu.cn; Dr. Mahalingam Ravivarma, State Key Laboratory for Mechanical Behavior of Materials, Shaanxi International Research Center for Soft Matter, School of Materials Science and Engineering, Xi'an Jiaotong University, Xi'an 710049, Shaanxi, China. E-mail: ravivarma@xjtu.edu.cn; Prof. Duanyang Kong, State Key Laboratory of Chemical Resource Engineering, Beijing University of Chemical Technology, Beijing 100029, China. E-mail: kongdy@buct.edu.cn

How to cite this article: Hu, F.; Cui, Z.; Dong, Z.; Jiang, L.; Njoku, N. N.; Dong, W.; Fan, H.; Ravivarma, M.; Wu, J.; Kong, D.; Song, J. Zwitterionic gemini additive as interface engineers for long-life aqueous Zn/TEMPO flow batteries with enhanced areal capacity. *Energy Mater.* **2025**, *5*, 500078. https://dx.doi.org/10.20517/energymater.2024.161

Received: 5 Sep 2024 **First Decision:** 11 Nov 2024 **Revised:** 2 Dec 2024 **Accepted:** 14 Dec 2024 **Published:** 28 Mar 2025

Academic Editor: Jiazhao Wang **Copy Editor:** Fangling Lan **Production Editor:** Fangling Lan

Abstract

Aqueous Zn-based flow batteries often face issues such as poor reversibility and short lifespan due to irregular Zn deposition and detrimental side reactions. To address these challenges, we developed a zwitterionic gemini additive, N,N′-bis(3-propanesulfonic acid)-3,3′-bipyridinium (SPr-Bpy), to enhance Zn plating/stripping behavior and optimize the Zn^{2+} solvation structure. The dual sulfonate groups influence the Zn^{2+} solvation shell and anchor SPr-Bpy to the Zn surface through multi-site interactions. Additionally, the bipyridinium structure forms an electrostatic shielding layer, suppressing excessive Zn^{2+} accumulation, promoting uniform Zn deposition, and thus mitigating dendrite formation and hydrogen evolution. Consequently, the Zn||Zn symmetric cells exhibit an impressive lifespan of 250 h, while the Zn||Cu asymmetric cells achieve a high average Coulombic efficiency of 99.8% over 450 cycles. Moreover, SPr-Bpy significantly improves Zn/TEMPO flow battery performance, achieving a high areal capacity of 24.4 mAh cm^{-2} with an exceptional capacity retention of 99.992%/cycle over 500 cycles.

Keywords: Zn/TEMPO flow batteries, interface engineering, zwitterionic gemini additive, electrostatic interaction, areal capacity

INTRODUCTION

With the continuous growth of the global economy and population, the demand for energy has surged, driving an increased reliance on renewable sources such as solar and wind energy[1-4]. However, optimal utilization of these renewables is hindered by the lack of cost-effective, long-duration energy storage technologies. To overcome the temporal and spatial limitations of renewable energy, developing advanced energy storage technologies has become a critical strategy for enabling more efficient and sustainable energy use[3,5-7]. Among these technologies, redox flow batteries (RFBs) have garnered significant interest as promising solutions for large-scale electrochemical energy storage. RFBs are particularly advantageous due to their flexible design options for power and capacity, long cycle life, fast response times, and environmentally friendly operation without harmful emissions[8,9].

Despite the commercialization of all-vanadium RFBs, their high cost remains a significant barrier to widespread adoption. This challenge underscores the urgent need for more affordable redox chemistries in aqueous RFBs. In response, various alternatives have been proposed, including metal-based[10,11], polysulfide-based[12-14], and organic RFBs[15-20]. Among these, aqueous Zn/Organic RFBs have emerged as a promising alternative due to their high safety, considerable energy density, affordability, and environmental friendliness, making them suitable for scalable energy storage[21-24]. However, aqueous Zn-based RFBs are prone to uncontrollable Zn dendrites on the electrodes, leading to rapid and irreversible capacity decay and potential short circuits[9,25,26]. Additionally, side reactions, such as hydrogen evolution reactions, frequently occur at the water-active interfaces of the Zn anode, causing significant pH changes and accelerating Zn anode corrosion[27-29]. To address these issues, several strategies have been explored, including the design of Zn-metal structures[30,31], the fabrication of artificial solid electrolyte interphases on Zn surfaces[32], separator modifications[9,33], the introduction of catalyst[34] and the incorporation of electrolyte additives[29,35]. Among them, the use of electrolyte additives stands out as the simplest, most efficient, and most practical solution due to their ease of application, low cost, and effectiveness in improving battery performance.

Electrolyte additives for aqueous Zn-based RFBs can be broadly classified into two categories based on their regulatory mechanisms. The first category comprises additives that interact on the surface to promote uniform Zn deposition and inhibit dendrite formation[36,37]. For instance, Yu *et al.* demonstrated that NH_4^+ acts as an effective inhibitor because its binding energy with the Zn surface is greater than that of Zn^{2+}, promoting more uniform Zn plating and reducing the risk of short circuits. The second category includes additives that modify the solvation structure of Zn^{2+}, thereby suppressing water-induced side reactions during cycling[27]. For example, Xu *et al.* identified N-Acetyl-ε-caprolactam (N-Ac) as a highly effective chelating agent[29]. By replacing a substantial portion of the water in the Zn^{2+} solvation shells, N-Ac minimizes water-related side reactions that typically lead to pH instability and Zn-anode corrosion. Furthermore, Geng *et al.* developed a class of hybrid aqueous electrolytes featuring an organic-solvent-free primary solvation shell, which leveraging the strong hydrogen bonds between CH_3COO^- and H_2O and the non-solvation effect of dimethyl sulfoxide, enabling facile desolvation and fast Zn^{2+} transport[38]. However, limited studies have explored multifunctional electrolyte additives capable of simultaneously regulating both the Zn interface and Zn^{2+} solvation structure. Further research in this area is needed.

Herein, we designed a novel zwitterionic gemini additive, N,N′-bis(3-propanesulfonic acid)-3,3′-bipyridinium (SPr-Bpy) [Supplementary Figure 1], simultaneously realizing homogeneous Zn^{2+} deposition and optimized Zn^{2+} solvation structure. Specifically, the dual sulfonate groups of SPr-Bpy not only partially displace the coordinated water molecules in the native Zn^{2+} solvation shell but also anchor the SPr-Bpy

molecule to the Zn surface through multi-site interactions, functioning similarly to a "pincer" to stabilize the additive on the electrode. As a result, the average coordination number of Zn-O (H_2O) decreases from approximately 6.0 to 5.7. Additionally, the bipyridinium structure of SPr-Bpy generates an electrostatic shielding layer on the Zn surface, creating electrostatic repulsion between SPr-Bpy and Zn^{2+}. This interaction effectively suppresses the excessive local accumulation of Zn^{2+}, promoting uniform Zn deposition while simultaneously suppressing dendrite formation and hydrogen evolution. These synergistic effects significantly improve the reversibility of Zn plating and stripping processes. This additive serves as an effective interface engineer for $ZnCl_2$ electrolytes in aqueous Zn/2,2,6,6-Tetramethylpiperidinyloxy (Zn/TEMPO) RFBs, representing a significant advancement in addressing critical challenges in Zn deposition and battery performance [Scheme 1]. Consequently, the assembled Zn/TEMPO RFB demonstrates a notable areal capacity of 24.4 mAh cm^{-2} and outstanding charge-discharge cycling stability over 500 cycles, with a remarkable capacity retention of 99.992%/cycle.

EXPERIMENTAL

Material preparation

The following reagents and solvents were used as received: Potassium chloride (Macklin), Zinc chloride (Macklin), 3-bromopyridine (Aladdin), 3-pyridylboronic acid (Aladdin), Potassium phosphate (Macklin), Pd_2dba_3 (Alfa Aesar), 2-dicyclohexylphosphine-2′, 6′-dimethoxybiphenyl (SPhos), dioxane (Aladdin), Anhydrous toluene, 3-propanesultone (Macklin), Zinc sheet (80 and 200 μm), CR2032 coin-cell, Glass fiber filter (GF/D, Whatman), and Anion-exchange membrane (AMVN, AGC).

Synthesis of N, N′-di(3-propane sulfonic acid)-3,3′-bipyridine (SPr-Bpy)

Synthesis of 3,3′-Bipyridine

The synthesis of 3,3′-bipyridine was conducted following a modified procedure[39] [Scheme 2A]. First, 3.36 g potassium phosphate was dissolved in 12 mL deionized water using ultrasonic agitation to facilitate dissolution, yielding a 1.27 mmol/L potassium phosphate stock solution. Next, 615 mg (5.0 mmol) 3-pyridylboronic acid, 40 mg Pd_2dba_3, 40 mg SPhos, and a stirring bar were placed into a flask. The flask was sealed with a septum, evacuated five times to remove air, and filled with nitrogen.

Subsequently, 380 μL (4.0 mmol) of 3-bromopyridine, 11.4 mL of dioxane, and 5.3 mL of the prepared potassium phosphate stock solution were added to the flask via a syringe. The resulting brown suspension was stirred and bubbled with nitrogen at room temperature for 15 min. The flask was then sealed with a Teflon valve and heated in an oil bath at 100 °C with continuous stirring for 18 h.

After the reaction was complete, the mixture was cooled to room temperature, filtered through diatomaceous earth, and washed with ethyl acetate to remove any residual substrate and catalyst. The product was extracted with ethyl acetate, concentrated under vacuum, and purified using silica gel column chromatography (eluent: CH_2Cl_2/MeOH = 1:0 to 20:1) to yield 3,3'-bipyridine.

Synthesis of SPr-Bpy

For the synthesis of SPr-Bpy, 1.46 g of 1,3-propanesultone (12 mmol) and 5 mL of anhydrous toluene were mixed in a reaction vessel and heated under a nitrogen atmosphere at reflux (110 °C) for 0.5 h. Subsequently, 0.78 g (5.0 mmol) of the synthesized 3,3'-bipyridine was gradually added to the reaction mixture with magnetic stirring to prevent precipitation and clumping. Following this, 2.4 mL of anhydrous toluene was added, and the reaction mixture was heated at 90 °C for an additional 11 h. After the reaction was complete, heating was discontinued, and the mixture was allowed to cool to room temperature. The product was then filtered and washed with toluene three times to ensure purity. Finally, the obtained white

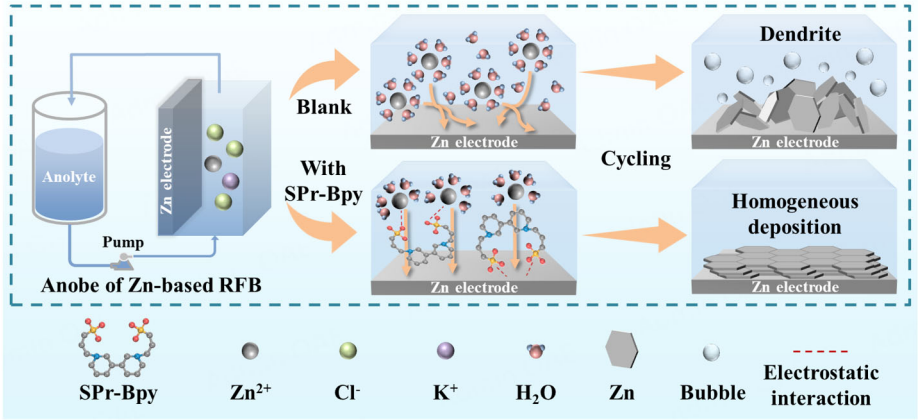

Scheme 1. Illustration of how the SPr-Bpy additive modulates Zn deposition behavior.

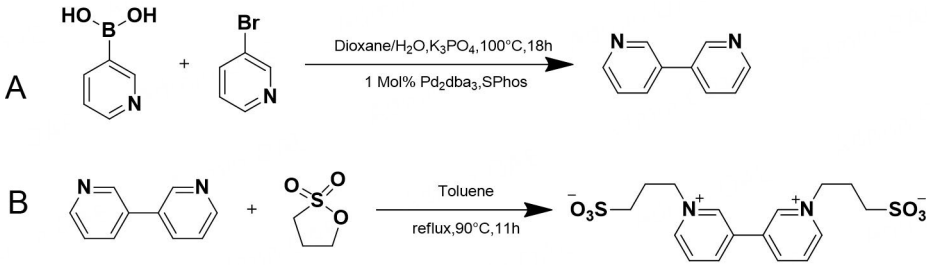

Scheme 2. The synthesis route of SPr-Bpy.

powder was dried under vacuum, yielding SPr-Bpy (1.94 g, 97% yield) [Scheme 2B]. ^{1}H NMR (600 MHz, D_2O) δ 9.45 (s, 1H), 9.15-9.08 (m, 1H), 8.95 (s, 1H), 8.36-8.28 (m, 1H), 4.93 (t, J = 7.5 Hz, 2H), 3.05 (s, 2H), 2.57 (s, 2H).

Characterizations

Nuclear magnetic resonance (NMR) spectra were recorded using a Bruker Avance-III HD 600 MHz spectrometer. X-ray diffraction (XRD) patterns were measured on the PANalytical Aeris X with Cu K_α radiation (λ = 0.15406 nm) and the test diffraction angle range was 2θ = 10°~80°. Ultraviolet-visible (UV-Vis) spectra were recorded on a UV-3600 plus spectrometer. Scanning Electron Microscope (SEM) images were captured using a Zeiss Gemini SEM 500 field emission microscope. The chemical states and atomic structure information were investigated by X-ray photoelectron spectroscopy (XPS) (Thermo Scientific K-Alpha).

Electrochemical measurements

The Zn||Zn symmetric cells, Zn||Cu asymmetric cells and Zn||V_2O_5 full cells were assembled in the CR2032 coin cells under an air atmosphere by using a glass fiber filter as the separator. A 0.5 M $ZnCl_2$ solution, both with and without an SPr-Bpy additive, served as the electrolyte. In the Zn||Zn symmetrical cells, two Zn foils (80 μm) were used as both the anode and cathode, whereas in the Zn||Cu asymmetric cells, the cathode was replaced with a Cu foil (20 μm). Zn||V_2O_5 full cells were assembled using Zn foils (80 μm) as the anode and V_2O_5 coated onto the stainless steel foil (20 μm) as the cathode. The V_2O_5, acetylene black and polyvinylidene fluoride (PVDF) were mixed in a N-methyl pyrrolidone solvent at a weight ratio of 7:2:1. The mass loadings of active material were about 2 mg cm^{-2}.

Cyclic voltammetry (CV) tests were carried out on an electrochemical workstation CHI 760e (CH Instruments, China) equipped with a three-electrode system in 1 M KCl aqueous solution. A polished glass carbon electrode was used as the working electrode, the platinum sheet as a counter electrode, and an Ag/AgCl (saturated KCl solution) electrode as the reference electrode. Electrolytes containing 5 mM $ZnCl_2$, with and without 0.25 mM SPr-Bpy in 1 M KCl, were measured with various scan rates of 25, 64, 100, 225, 400, and 625 mV s^{-1}. Linear polarization curves (LSV) were tested over a potential range of -0.90 to -1.24 V at a scan rate of 10 mV s^{-1}. Corrosion Tafel plots were recorded over a potential range of -0.15 to 0.15 V *vs.* Zn/Zn^{2+} at a scan rate of 10 mV s^{-1}. The diffusion coefficients (D/cm^2 s^{-1}) of the active species were determined by using the Randles-Sevcik equation[3]:

$$i_p = 2.69 \times 10^5 \times A\, n^{3/2}\, D^{1/2}\, C\, v^{1/2}$$

where i_p is the peak current from the CV testing, A is the electrode reaction area, n is the number of electrons involving the redox process, D is the diffusion coefficient, C is the concentration of compounds, and v is the scan rate in mV s^{-1}.

Flow battery tests

The flow battery tests were performed under a battery test system (CT-4008-5V6A-S1-F, Neware, Shenzhen, China) at room temperature. The assembly of the battery followed a specific sequence: a fixed frame, PTFE block, a zinc sheet (200 μm) serving as the anode, a graphite felt electrode, rubber seal, anion-exchange membrane (AMVN) as a separator, another rubber seal, a second graphite felt electrode, a graphite plate fluid collector, a copper collector, and finally another fixed frame. For the long-term cycling test, two different anolytes were used: 10 mL 0.5 M $ZnCl_2$ with and without 0.025 M SPr-Bpy, both in 1 M KCl. The catholyte consisted of 10 mL 0.5 M 4-(3-(trimethylammonium)acetylamino)-2,2,6,6-tetramethylpiperidine-1-oxyl chloride (TMAAcNH-TEMPO)[6] in 1 M KCl. The electrolytes were pumped into the cell at a flow rate of 60 mL min^{-1} through a peristaltic pump (BT300M, Baoding Chuang Rui Precision Pump Co., Ltd.) under open-air atmosphere. The active areas of both the electrode and the separator were 5 cm^2. The full batteries were conducted in the voltage range from 1.2 to 2.0 V with a galvanostatic-potentiostatic system at a current density of 20 mA cm^{-2} until the current density decreased to 3 mA cm^{-2}.

Theoretical calculation

Molecular dynamics (MD) simulations were conducted using the large-scale atomic/molecular massively parallel simulator (LAMMPS) code (ver. 29 Sep 2021). The forced field parameters were obtained from the optimized potentials for liquid simulations-all atom (OPLS-AA) force fields. The extended simple point charge (SPC/E) water model is employed for H_2O molecules. Advanced restrained electrostatic potential (RESP2) atomic partial charges were obtained based on electrostatic potential (ESP) charges calculated using Multiwfn (ver. 3.8dev). The initial atomic coordinates were generated with PACKMOL (ver. 20.010), and the MD snapshots were visualized with VESTA (ver. 3.5.7).

Firstly, all electrolyte models were equilibrated in an isothermal-isobaric (constant NPT) ensemble using the Parrinello-Rahman barostat for 2.0 ns to maintain a temperature of 298 K and a pressure of 1 atm. After that, the electrolytes were heated from 298 to 500 K within 0.5 ns, maintained at 500 K for 1.0 ns, and then cooled from 500 to 298 K within 0.5 ns, followed by equilibration at 298 K for another 2 ns. A 2 ns production run was finally conducted in the canonical (constant NVT) ensemble under the Nose-Hoover thermostat.

The radial distribution function $g(r)$ was obtained from the trajectory files. The coordination numbers of the Zn^{2+} and solvents were calculated by

$$N = \int_0^r 4\pi r^2 g(r) dr$$

where ρ and r represent the number density of coordination atoms and the distance between the coordination atom and the reference atom, respectively.

The calculation related to the interaction between Zn crystal and molecules was performed by the density functional theory (DFT) program Device Studio Projector Augmented Wave (DS-PAW). The exchange-correlation functional within the Perdew, Burke, and Ernzerhof (PBE) generalized gradient approximation (GGA) was used to handle the interactions between electrons. The DFT-D3 method was employed to calculate the van der Waals (vdW) interactions. The positions of all atoms and the lattice constants were optimized using the conjugate gradient algorithm. The convergence criteria for the energy and force of each atom were set to less than 1×10^{-5} eV and 0.01 eV/Å, respectively. The plane wave energy cutoff for the electronic wavefunction expansion was set to 500 eV. A 3 × 3 × 3 k-point mesh was used for Brillouin zone integration. A vacuum layer of 20 Å was applied in the direction vertical to the surface to eliminate interactions between adjacent images. The positions of all atoms and the lattice constants were fully optimized using the conjugate gradient algorithm. In the convergence tolerance, the energy, force, and displacement were set as 10^{-6} Ha, 0.01 Ha/Å, and 0.005 Å, separately. The adsorption energy (E_a) of SPr-Bpy on different Zn planes (100), (101) and (002) can be defined as

$$E_a = E_{SPr@Zn} - E_{Zn} - E_{SPr}$$

Here, $E_{SPr@Zn}$ represents the energy of the SPr-Bpy adsorbed on the Zn surface in implicit solvent water ($\varepsilon = 78.4$), E_{Zn} stands for the energy of the Zn surface, and E_{SPr} indicates the energy of the SPr-Bpy molecule.

RESULTS AND DISCUSSION

Electrochemical characterization of electrolyte with/without SPr-Bpy

CV tests were initially performed to evaluate the impact of SPr-Bpy additives on the electrochemical behavior of the Zn^{2+}/Zn redox couple. The results demonstrated that the presence of SPr-Bpy significantly influenced the Zn^{2+}/Zn redox performance [Figure 1A]. Without any additive, the blank electrolyte displayed an average potential of -1.00 V (*vs.* sat. Ag/AgCl) with a peak-to-peak separation of 580 mV. Upon the addition of SPr-Bpy, the oxidation potential shifted negatively by approximately 140 mV, resulting in an overall decrease of 40 mV in the redox potential. More importantly, the peak-to-peak separation decreased to 420 mV, indicating a substantial improvement in redox reversibility. To further investigate the electrochemical property, a series of CV curves were analyzed at various scan rates ranging from 25 to 625 mV/s [Figure 1B]. The linear relationship observed between the peak current and the square root of the scan rate suggested a diffusion-controlled process. According to the Randles-Sevcik equation, the diffusion coefficients for the oxidation and reduction reactions were determined to be 4.32×10^{-12} and 4.68×10^{-12} cm^2/s, respectively. The close similarity between these values further confirmed the high redox reversibility of the Zn^{2+}/Zn redox couple in the presence of the SPr-Bpy additive.

Furthermore, linear sweep voltammetry (LSV) tests were carried out to assess the effect of SPr-Bpy on hydrogen evolution during Zn deposition. The LSV curves showed that the introduction of SPr-Bpy caused

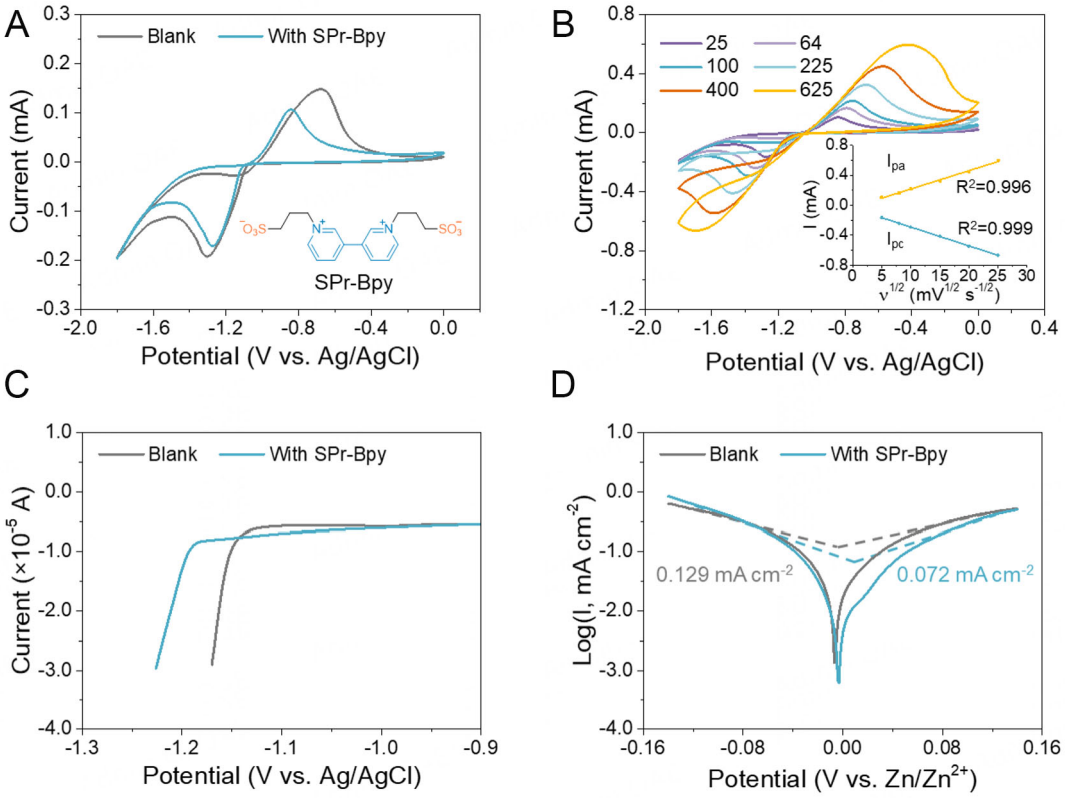

Figure 1. Electrochemical measurements of $ZnCl_2$ electrolytes with and without SPr-Bpy. (A) CV profiles of 5 mM $ZnCl_2$ with 0.25 mM SPr-Bpy (blue) at 25 mV s^{-1}. The blank case without SPr-Bpy (grey) is presented for comparison. Inset: molecular structure of SPr-Bpy. (B) CV curves at various scan rates. Inset: linear fit of peak current *vs.* the square root of scan rate. (C and D) LSV results (C) and Tafel curves (D) in 0.5 M $ZnCl_2$ with 25 mM SPr-Bpy (blue) and blank group (grey) at 10 mV s^{-1}.

a negative shift in the HER potential, indicating effective suppression of HER by SPr-Bpy. This shift increased with concentration, reaching saturation at 25 mM, where the HER potential shifted from -1.15 V to around -1.20 V [Figure 1C]. Further increases in the additive concentration had minimal impact on the HER potential [Supplementary Figure 2].

To further evaluate the effect of SPr-Bpy on corrosion and side reactions, Tafel curve analysis was employed. The electrolyte containing SPr-Bpy exhibited a lower corrosion current density of 0.072 mA cm^{-2}, compared to 0.129 mA cm^{-2} for the blank electrolyte, demonstrating that SPr-Bpy effectively reduced the corrosion tendency and rate of Zn, likely due to its protective effect [Figure 1D]. For subsequent battery testing, CV tests were conducted using 0.5 M $ZnCl_2$ solutions with and without additives. The results were consistent with those obtained at lower concentrations, supporting the decision to assemble both symmetric and asymmetric cells for additional evaluation [Supplementary Figure 3].

The changes in electrochemical behavior induced by the additive may stem from its influence on the solvation structure of Zn^{2+}. To further verify the infer, we performed MD simulations to analyze the solvation structure of Zn^{2+} in the presence of SPr-Bpy. As shown in Supplementary Figure 4, SPr-Bpy significantly influences the solvation shell of Zn^{2+} through electrostatic interactions between its zwitterionic structure and Zn^{2+}. To further quantify these effects, we obtained the corresponding radial distribution functions (RDFs) and coordination number analysis for different electrolyte models, providing a detailed insight into the solvation structure of Zn^{2+}. In both the SPr-Bpy-containing and blank $ZnCl_2$ electrolyte

solutions, a sharp peak of the Zn-O (H_2O) appears at approximately r = 2.1 Å, corresponding to the coordination of H_2O around Zn^{2+}. However, in the presence of SPr-Bpy, a new, intense peak appears at r = 1.9 Å, representing Zn-O (SO_3) interactions, indicating a direct interaction between SPr-Bpy and Zn^{2+}. Furthermore, the average coordination number of Zn-O (H_2O) decreases from near 6.0 to 5.7, suggesting that some H_2O molecules are replaced with the insertion of the SPr-Bpy into the solvation shell of Zn^{2+} [Supplementary Figure 5].

Battery performance test of electrolyte with/without SPr-Bpy

To investigate the impact of the SPr-Bpy additive on cycling stability of the Zn anode, Zn||Zn symmetric cells were first assembled and tested under various conditions. To evaluate the impact of the SPr-Bpy additive on the cycling stability of the battery more efficiently, we conducted rate performance tests under current densities ranging from 1 to 8 mA cm^{-2} [Supplementary Figure 6] and selected 6 mA cm^{-2} as a relatively demanding condition for further cell testing. Different concentrations of SPr-Bpy, ranging from 5 to 100 mM, were added into 0.5 M $ZnCl_2$ to identify the optimal concentration for achieving stable long-term cycling performance [Figure 2A]. Notably, SPr-Bpy exhibited irreversible electrochemical behavior and, therefore, does not directly contribute to the capacity [Supplementary Figure 7]. Among the tested concentrations, 25 mM SPr-Bpy showed the most significant improvement in battery lifespan, maintaining stable operation for nearly 250 h at 1 mAh cm^{-2} and 6 mA cm^{-2}. This performance represents a more than threefold increase in lifespan compared to the approximately 60 h observed for cells without SPr-Bpy (blank). Interestingly, the addition of SPr-Bpy to the $ZnCl_2$ electrolyte led to an increase in polarization voltage during the initial period, which subsequently stabilized to maintain a consistent cell voltage.

To further evaluate the impact of the SPr-Bpy additive on the reversibility of Zn stripping/plating during charge and discharge, Zn||Cu asymmetric cells were also tested. For the blank electrolyte, the Zn||Cu cell exhibited an overpotential of approximately 100 mV at 1 mAh cm^{-2} and 6 mA cm^{-2}. In contrast, with the addition of 25 mM SPr-Bpy, the Zn||Cu cell exhibited a higher overpotential of approximately 150 mV, which is 50 mV greater than that of the blank electrolyte [Figure 2B and C]. This observation aligns with the increased polarization noted in the Zn||Zn symmetric cells. Despite the increase in overpotential, the Coulombic efficiency (CE) of Zn^{2+} plating/stripping showed significant improvements in cycling stability [Figure 2D]. The Zn||Cu cell with the blank electrolyte displayed a sharp decrease in CE after 105 cycles due to issues such as dendrite-induced short circuits. In contrast, the Zn||Cu cell with 25 mM SPr-Bpy exhibited remarkable stability, maintaining an average CE of 99.8% over 450 cycles, compared to 99.3% for the blank. This enhanced CE demonstrates the effectiveness of SPr-Bpy in promoting stable Zn deposition processes. The Zn||V_2O_5 full cells were further assembled to confirm the regulation effect of SPr-Bpy. As demonstrated in Supplementary Figure 8, the Zn||V_2O_5 full cell with SPr-Bpy achieved a more stable cycling performance with capacity decay of 0.18%/cycle over 200 cycles at 5 A g^{-1} compared to the Blank (0.45%/cycle over 100 cycles).

To investigate the origin of the observed effects, we analyzed the interaction between SPr-Bpy and the Zn surface by calculating the E_a of SPr-Bpy on Zn. As shown in Supplementary Figure 8, the dual sulfonate chains on the SPr-Bpy molecular structure act as binding sites for Zn, anchoring the molecule firmly to the Zn surface. Simultaneously, the positively charged bipyridinium structure of SPr-Bpy induces the formation of an electrostatic shielding layer around the Zn protuberance to induce uniform Zn deposition [Supplementary Figure 9][35]. Furthermore, we found that the adsorption energies of SPr-Bpy on the Zn (100) and (101) planes are significantly higher than that on the Zn (002) plane, leading to an increased nucleation barrier on the Zn (100) and (101) planes, thereby promoting Zn^{2+} selectively deposition on the Zn (002) plane[40].

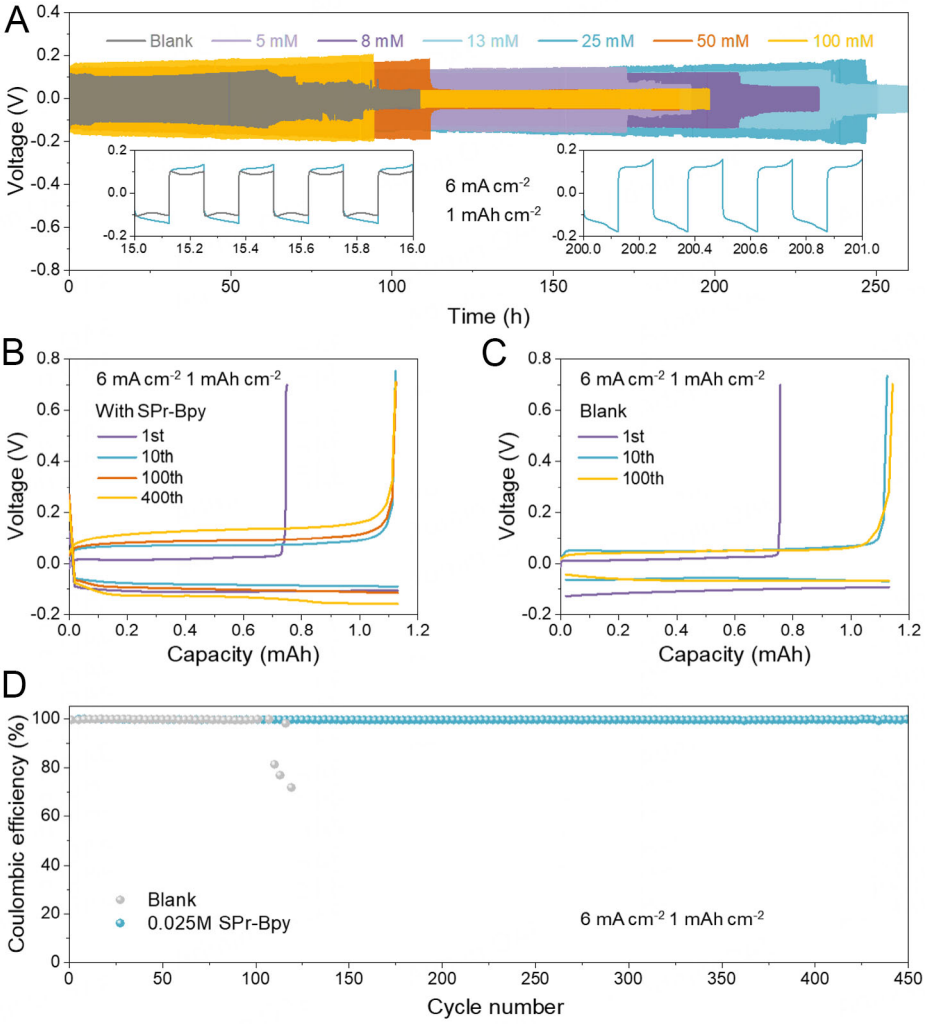

Figure 2. Performance of Zn||Zn symmetric and Zn||Cu asymmetric coin cells with/without SPr-Bpy in 0.5 M $ZnCl_2$. (A) Long-term cycling of Zn||Zn symmetric cells with various concentrations of SPr-Bpy. (B and C) Voltage-capacity curves of Zn||Cu cells under different cycle numbers (B) with 25 mM SPr-Bpy and (C) Blank electrolytes. (D) The corresponding CE plots with respect to the cycle number of Zn||Cu cells.

Characterization of cells with/without SPr-Bpy after cycling

SEM was employed to observe the surface morphology of the Zn electrode before and after the battery operation. SEM images showed a substantial amount of irregularly arranged Zn flakes on the surface of the Zn anode after cycling in the blank electrolyte [Figure 3A]. These Zn flakes displayed large-angle growth with respect to the Zn substrate, facilitating the formation of dendrites. In comparison, when Zn was cycled in $ZnCl_2$ electrolyte containing the SPr-Bpy additive, the surface exhibited a more uniform Zn distribution. The deposited Zn showed smaller angles relative to the substrate, demonstrating a suppression of side reactions [Figure 3B and Supplementary Figure 10].

Additionally, XRD analysis revealed notable changes in the diffraction peaks corresponding to the (002), (100), (101) and other Zn crystal planes with and without SPr-Bpy additives [Figure 3C]. The intensity ratio of (002)/(100) diffraction peaks increased to 3.07 in an additive-containing electrolyte, compared to 1.23 in the blank case, indicating a preferential growth of the (002) crystal plane. Furthermore, a series of new peaks, denoted by "#", were detected on the surface of the Zn electrode after cycling, which were

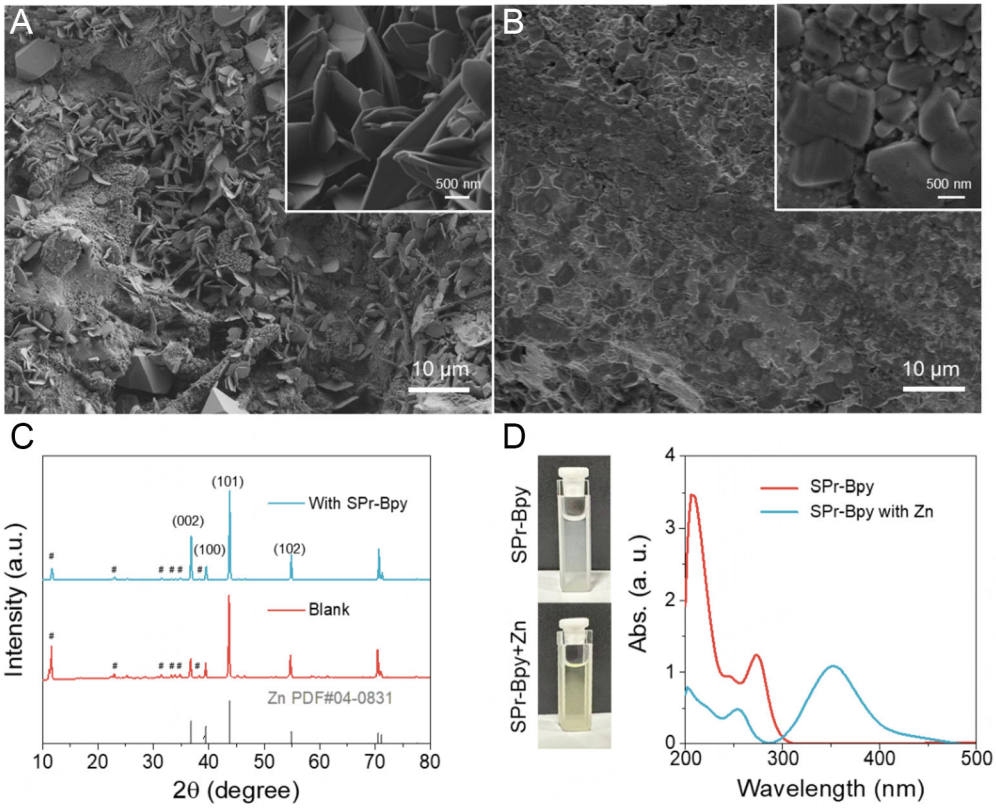

Figure 3. The characterizations of Zn anode after cycling in different electrolytes. (A and B) SEM images of the Zn anode in (A) blank and (B) SPr-Bpy-containing electrolytes after cycling. (C) The corresponding XRD patterns of blank and SPr-Bpy-containing electrolytes. (D) UV-Vis spectra of SPr-Bpy before and after the addition of Zn.

preliminarily identified as the zinc hydroxide chloride, $Zn_5(OH)_8Cl_2{\cdot}H_2O$ [Supplementary Figure 11]. Notably, the Zn metal in the SPr-Bpy/$ZnCl_2$ electrolyte displayed weaker $Zn_5(OH)_8Cl_2{\cdot}H_2O$ peaks than the blank group, underscoring the additive's protective effect on the Zn anode.

To further investigate the interactions between the multi-site structure of SPr-Bpy and Zn, UV-Vis spectroscopy was conducted to evaluate the effect of the SPr-Bpy additive on the electrode. The UV-Vis spectra of SPr-Bpy exhibited two distinct absorption peaks at 210 and 275 nm. Upon the addition of Zn to the SPr-Bpy solution, these original absorption peaks significantly decreased in intensity, and a new peak emerged at 354 nm [Figure 3D]. The red shift of UV-Vis peaks may be attributed to the electrostatic attraction between dual sulfonates on SPr-Bpy and Zn. Specifically, this interaction redistributes the electron density within the molecule, reducing the overall electron density of SPr-Bpy.

We then compared the XPS spectra of pristine Zn and SPr-Bpy-adsorbed Zn after 50 charge-discharge cycles to analyze the interaction form between the Zn and SPr-Bpy. After adding SPr-Bpy, as shown in Supplementary Figure 12, the wide-scan XPS spectra demonstrate the presence of a trace amount of S (1.72%). S 2p peaks appearing at 168.2 and 169.3 eV in Supplementary Figure 13 correspond to C-S and S=O, respectively[41]. Meanwhile, in Supplementary Figure 14, the same peak positions of Zn 2p spectra for pristine Zn and SPr-Bpy -added Zn at 1,021.7 and 1,044.9 eV correspond to the form of Zn^{2+}[42], further demonstrating that the interaction mainly originates from the electrostatic attraction of SPr-Bpy on the Zn electrode surface while not the chemical reaction.

These findings confirm that SPr-Bpy effectively regulates the Zn deposition behavior during cycling, promoting the growth of the Zn (002) crystal plane as the dominant orientation.

Battery performance of Zn/TEMPO RFBs

After confirming the cycling stability of the previously discussed cells, we proceeded to test the flowable Zn/TEMPO RFBs under various conditions to evaluate the practical effectiveness of the SPr-Bpy additive. The experimental setup for these tests is depicted in Figure 4A. The Zn/TEMPO RFB was assembled using 0.05 M TMAAcNH-TEMPO as the catholyte and 0.05 M $ZnCl_2$, with and without SPr-Bpy, as the anolyte. Owing to the favorable redox potentials of Zn^{2+} (-1.04 V with SPr-Bpy *vs.* sat. Ag/AgCl) and TMAAcNH-TEMPO (0.64 V *vs.* sat. Ag/AgCl) [Supplementary Figure 15], the setup achieved a high open-circuit voltage close to 1.70 V [Supplementary Figure 16]. The addition of SPr-Bpy resulted in a significant reduction in capacity decay to less than 1% and an increase in CE to over 99.5% within 100 cycles, compared to over 20% capacity decay and less than 98.0% CE in the blank case [Supplementary Figures 17 and 18].

We then explored the performance of high-concentration batteries using 10 mL 0.5 M TMAAcNH-TEMPO catholyte and 10 mL 0.5 M $ZnCl_2$ anolyte. In the case of the blank electrolyte, the RFB exhibited a sharp decline in cycling stability, with discharge capacity reducing by over 30% after just 80 cycles [Figure 4B]. In contrast, the RFB with SPr-Bpy additive demonstrated significant improvements in both stability and efficiency, maintaining a nearly perfect CE of close to 100% and EE of nearly 70% over 500 cycles. This highlights the profound impact of the additive on battery performance.

Moreover, while the polarization increased steadily during cycling, the potentiostatic parts of the battery operation remained nearly stable. These improvements are attributed to the multifaceted role of the SPr-Bpy additive, which regulates Zn^{2+} solvation structure and promotes a more uniform Zn deposition surface, thereby preventing dendrite formation. The zwitterionic and gemini properties of the additive facilitate a balanced interaction with Zn^{2+}, reducing localized charge imbalances and promoting smooth and controlled Zn plating and stripping. Consequently, the presence of SPr-Bpy minimizes parasitic reactions such as HER and Zn corrosion, which commonly degrade battery performance over extended cycles.

The RFB with SPr-Bpy also demonstrated superior performance under high areal capacity conditions. It achieved a high areal capacity of 24.4 mAh cm^{-2} with a minimal capacity fade rate of only 0.08%/cycle, which is substantially lower than that of similar Zn-based RFBs without additives [Figure 4C][22,43-49]. This performance is particularly noteworthy because high areal capacities are often associated with increased risks of Zn dendrite formation and electrolyte instability, which can lead to rapid capacity fade and reduced cycle life. The ability of the SPr-Bpy additive to maintain structural and electrochemical stability even at high capacities underscores its potential as a key component in advancing next-generation energy storage technologies. It highlights the additive's efficacy in enhancing both the mechanical robustness and electrochemical resilience of the Zn/TEMPO RFBs, making it a promising candidate for large-scale energy storage applications where high capacity and long-term reliability are paramount.

CONCLUSION

In summary, we synthesized a zwitterionic gemini additive, SPr-Bpy, featuring dual cationic and anionic sites, as an innovative interface engineer for aqueous $ZnCl_2$ electrolytes in Zn/TEMPO RFBs. The unique multi-site structure of SPr-Bpy played a critical role in significantly enhancing the Zn^{2+}/Zn redox reaction by optimizing solvation and diffusion, which reduced dendrite formation and improved the uniformity of Zn deposition. Experimental findings demonstrated that SPr-Bpy effectively mitigated hydrogen evolution and reduced corrosion, thereby contributing to enhanced cycling stability. The improved cycling

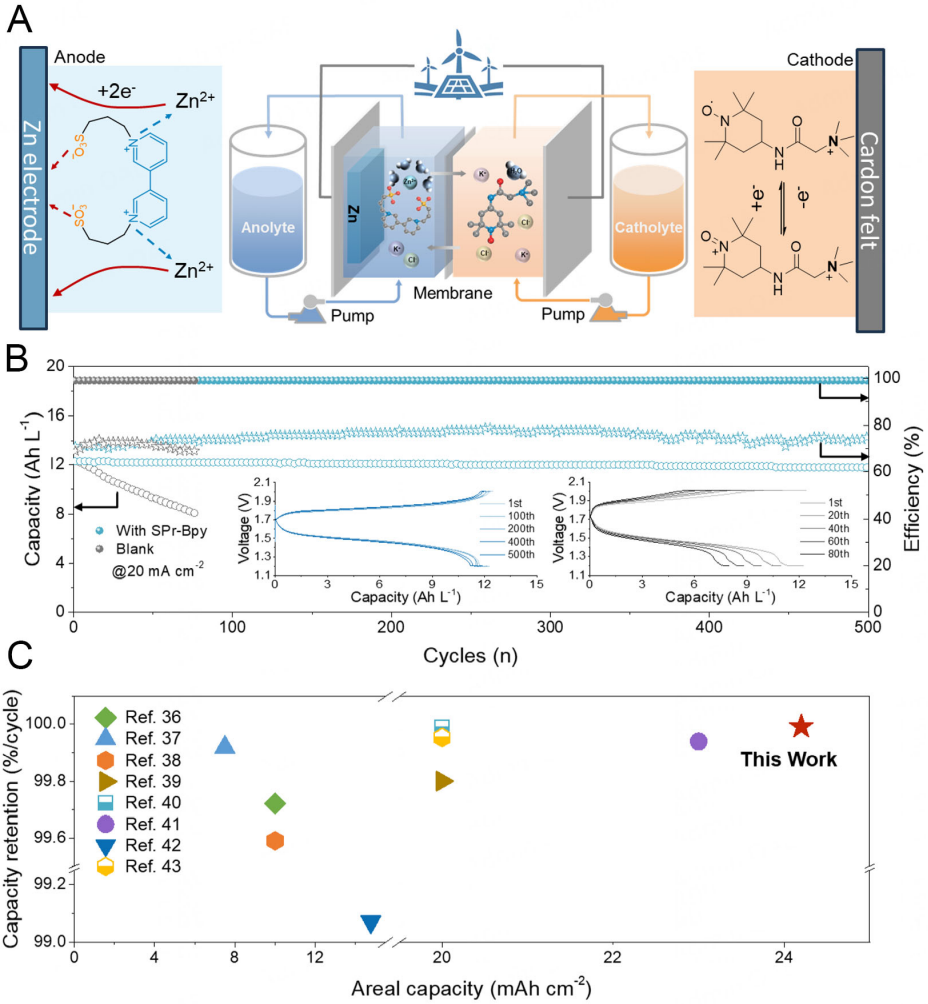

Figure 4. Performance of assembled Zn/TEMPO RFB with 0.5 M $ZnCl_2$ (with and without 0.025 M SPr-Bpy) in anolyte and 0.5 M TMAAcNH-TEMPO in catholyte. 1 M KCl was used as supporting electrolytes. (A) Diagram and mechanism of Zn/TEMPO RFB with SPr-Bpy. (B) Long-term cycling of the battery with an areal capacity of 24.4 mAh cm^{-2}. The battery was cycled galvanostatically at 20 mA cm^{-2} and ended with a potentiostatic hold until the magnitude of the current density fell below 3.0 mA cm^{-2}. Inset: Voltage-capacity curve of the RFBs with and without SPr-Bpy. (C) Comparison of the battery performance of this work with that of other reported Zn-based RFBs. Key parameters of battery capacity retention and areal capacity are compared.

performance observed in both Zn||Zn symmetric and Zn||Cu asymmetric cells highlighted the additive's effectiveness in extending cycle life and increasing CE. Complementary SEM and XRD analyses confirmed that SPr-Bpy promoted the preferential growth of the (002) crystal plane, resulting in more controlled and uniform Zn deposition. The Zn/TEMPO RFBs utilizing SPr-Bpy exhibited exceptional long-term stability, maintaining near 100% CE over 500 cycles and achieving a high areal capacity with minimal capacity degradation. Overall, the introduction of SPr-Bpy represents a promising advancement in electrolyte additives for Zn-based RFBs, addressing key challenges in Zn deposition and battery performance, and paving the way for more efficient and durable energy storage solutions.

DECLARATIONS

Authors' contributions

Made substantial contributions to the conception and design of the study and performed data analysis and interpretation: Hu, F.; Fan, H.

Performed data acquisition: Hu, F.; Cui, Z.; Dong, Z.; Njoku, N. N.
Provided technical and material support: Hu, F.; Cui, Z.; Dong, Z.; Njoku, N. N.
Wrote the first version of the manuscript: Hu, F.; Dong, W.
Managed the project: Fan, H.; Ravivarma, M.; Kong, D.; Song, J.
Reviewed and revised the manuscript: Hu, F.; Cui, Z.; Dong, Z.; Jiang, L.; Njoku, N. N.; Dong, W.; Fan, H.; Ravivarma, M.; Wu, J.; Kong, D.; Song, J.

Availability of data and materials

Some data are presented in the "Supplementary Materials" section. Other raw data that support the findings of this study are available from the corresponding author upon reasonable request.

Financial support and sponsorship

This work was financially supported by the National Natural Science Foundation (No. 22209130, No. 22279100 and No. 22101018), the Beijing Nova Program (No. Z211100002121126 and No. 20230484447), and the State Key Laboratory for Mechanical Behavior of Materials (No. 20222407).

Conflicts of interest

Fan, H. is Guest Editor of the Special Issue of "Key Materials for Aqueous Flow Battery" of the journal *Energy Materials*, and he is not involved in any steps of editorial processing, notably including reviewers' selection, manuscript handling and decision making. Dong, Z. is affiliated with Shaanxi Coal Chemical Industry Technology Research Institute Co. Ltd., while the other authors have declared that they have no conflicts of interest.

Ethical approval and consent to participate

Not applicable.

Consent for publication

Not applicable.

REFERENCES

1. Moutet, J.; El-Assaad, T. H.; Kaur, R.; Mills, D. D.; Gianetti, T. L. Designing the next generation of symmetrical organic redox flow batteries using helical carbocations. *Energy. Mater.* **2024**, *4*, 400024. DOI
2. Zhang, J.; Lejarazu-Larrañaga, A.; Yang, F.; et al. Tailoring porous structure in non-ionic polymer membranes using multiple templates for low-cost iron-lead single-flow batteries. *Energy. Mater.* **2024**, *4*, 400042. DOI
3. Fan, H.; Liu, K.; Zhang, X.; et al. Spatial structure regulation towards armor-clad five-membered pyrroline nitroxides catholyte for long-life aqueous organic redox flow batteries. *eScience* **2024**, *4*, 100202. DOI
4. Zuo, L. L.; Ma, Q.; Li, S. C.; et al. Highly thermal conductive separator with in-built phosphorus stabilizer for superior Ni-rich cathode based lithium metal batteries. *Adv. Energy. Mater.* **2021**, *11*, 2003285. DOI
5. Li, H.; Fan, H.; Hu, B.; Hu, L.; Chang, G.; Song, J. Spatial structure regulation: a rod-shaped viologen enables long lifetime in aqueous redox flow batteries. *Angew. Chem. Int. Ed.* **2021**, *60*, 26971-7. DOI
6. Fan, H.; Wu, W.; Ravivarma, M.; et al. Mitigating ring-opening to develop stable TEMPO catholytes for pH-neutral all-organic redox flow batteries. *Adv. Funct. Mater.* **2022**, *32*, 2203032. DOI
7. Duan, Y.; Li, B.; Yang, K.; et al. Ultrahigh energy and power density in Ni-Zn aqueous battery via superoxide-activated three-electron transfer. *Nanomicro. Lett.* **2024**, *17*, 79. DOI PubMed PMC
8. Li, Z.; Lu, Y. C. Material design of aqueous redox flow batteries: fundamental challenges and mitigation strategies. *Adv. Mater.* **2020**, *32*, e2002132. DOI
9. Zhao, C. X.; Liu, J. N.; Li, B. Q.; et al. Multiscale construction of bifunctional electrocatalysts for long-lifespan rechargeable zinc-air batteries. *Adv. Funct. Mater.* **2020**, *30*, 2003619. DOI
10. Huang, Y.; Li, L.; Xiong, L.; et al. Electrodes with metal-based electrocatalysts for redox flow batteries in a wide pH range. *Prog.*

Energy. **2023**, *5*, 022002. DOI
11. Amini, K.; Gostick, J.; Pritzker, M. D. Metal and metal oxide electrocatalysts for redox flow batteries. *Adv. Funct. Mater.* **2020**, *30*, 1910564. DOI
12. Li, Z.; Weng, G.; Zou, Q.; Cong, G.; Lu, Y. C. A high-energy and low-cost polysulfide/iodide redox flow battery. *Nano. Energy.* **2016**, *30*, 283-92. DOI
13. Ma, D.; Hu, B.; Wu, W.; et al. Highly active nanostructured CoS_2/CoS heterojunction electrocatalysts for aqueous polysulfide/iodide redox flow batteries. *Nat. Commun.* **2019**, *10*, 3367. DOI PubMed PMC
14. Xia, Y.; Ouyang, M.; Yufit, V.; et al. A cost-effective alkaline polysulfide-air redox flow battery enabled by a dual-membrane cell architecture. *Nat. Commun.* **2022**, *13*, 2388. DOI PubMed PMC
15. Ai, F.; Wang, Z.; Lai, N. C.; Zou, Q.; Liang, Z.; Lu, Y. C. Heteropoly acid negolytes for high-power-density aqueous redox flow batteries at low temperatures. *Nat. Energy.* **2022**, *7*, 417-26. DOI
16. Amini, K.; Kerr, E. F.; George, T. Y.; et al. An extremely stable, highly soluble monosubstituted anthraquinone for aqueous redox flow batteries. *Adv. Funct. Mater.* **2023**, *33*, 2211338. DOI
17. Carrington, M. E.; Sokołowski, K.; Jónsson, E.; et al. Associative pyridinium electrolytes for air-tolerant redox flow batteries. *Nature* **2023**, *623*, 949-55. DOI PubMed PMC
18. Feng, R.; Chen, Y.; Zhang, X.; et al. Proton-regulated alcohol oxidation for high-capacity ketone-based flow battery anolyte. *Joule* **2023**, *7*, 1609-22. DOI
19. Hu, M.; Wu, W.; Luo, J.; Liu, T. L. Desymmetrization of viologen anolytes empowering energy dense, ultra stable flow batteries toward long-duration energy storage. *Adv. Energy. Mater.* **2022**, *12*, 2202085. DOI
20. Jing, Y.; Zhao, E. W.; Goulet, M. A.; et al. In situ electrochemical recomposition of decomposed redox-active species in aqueous organic flow batteries. *Nat. Chem.* **2022**, *14*, 1103-9. DOI
21. Na, M.; Singh, V.; Choi, R. H.; Kim, B. G.; Byon, H. R. Zn glutarate protective layers in situ form on Zn anodes for Zn redox flow batteries. *Energy. Storage. Mater.* **2023**, *57*, 195-204. DOI
22. Park, M.; Beh, E. S.; Fell, E. M.; et al. A high voltage aqueous zinc-organic hybrid flow battery. *Adv. Energy. Mater.* **2019**, *9*, 1900694. DOI
23. Xiang, W.; Yang, M.; Ding, M.; et al. Alkaline Zn-Mn aqueous flow batteries with ultrahigh voltage and energy density. *Energy. Storage. Mater.* **2023**, *61*, 102894. DOI
24. Yuan, Z.; Li, X. Perspective of alkaline zinc-based flow batteries. *Sci. China. Chem.* **2024**, *67*, 260-75. DOI
25. Zhu, Y.; Liang, G.; Cui, X.; et al. Engineering hosts for Zn anodes in aqueous Zn-ion batteries. *Energy. Environ. Sci.* **2024**, *17*, 369-85. DOI
26. Dong, N.; Zhang, F.; Pan, H. Towards the practical application of Zn metal anodes for mild aqueous rechargeable Zn batteries. *Chem. Sci.* **2022**, *13*, 8243-52. DOI PubMed PMC
27. Yu, H.; Chen, D.; Ni, X.; et al. Reversible adsorption with oriented arrangement of a zwitterionic additive stabilizes electrodes for ultralong-life Zn-ion batteries. *Energy. Environ. Sci.* **2023**, *16*, 2684-95. DOI
28. Zhou, S.; Meng, X.; Chen, Y.; et al. Zinc-ion anchor induced highly reversible Zn anodes for high performance Zn-ion batteries. *Angew. Chem. Int. Ed.* **2024**, *63*, e202403050. DOI
29. Xu, D.; Ren, X.; Li, H.; et al. Chelating additive regulating Zn-ion solvation chemistry for highly efficient aqueous zinc-metal battery. *Angew. Chem. Int. Ed.* **2024**, *63*, e202402833. DOI
30. Qin, R.; Wang, Y.; Yao, L.; et al. Progress in interface structure and modification of zinc anode for aqueous batteries. *Nano. Energy.* **2022**, *98*, 107333. DOI
31. Yuan, L.; Hao, J.; Kao, C. C.; et al. Regulation methods for the Zn/electrolyte interphase and the effectiveness evaluation in aqueous Zn-ion batteries. *Energy. Environ. Sci.* **2021**, *14*, 5669-89. DOI
32. Zhao, Q.; Stalin, S.; Archer, L. A. Stabilizing metal battery anodes through the design of solid electrolyte interphases. *Joule* **2021**, *5*, 1119-42. DOI
33. Zhao, Z.; Wang, R.; Peng, C.; et al. Horizontally arranged zinc platelet electrodeposits modulated by fluorinated covalent organic framework film for high-rate and durable aqueous zinc ion batteries. *Nat. Commun.* **2021**, *12*, 6606. DOI
34. Dai, Y.; Lu, R.; Zhang, C.; et al. Zn^{2+}-mediated catalysis for fast-charging aqueous Zn-ion batteries. *Nat. Catal.* **2024**, *7*, 776-84. DOI
35. Han, D.; Wang, Z.; Lu, H.; et al. A self-regulated interface toward highly reversible aqueous zinc batteries. *Adv. Energy. Mater.* **2022**, *12*, 2102982. DOI
36. Bayaguud, A.; Luo, X.; Fu, Y.; Zhu, C. Cationic surfactant-type electrolyte additive enables three-dimensional dendrite-free zinc anode for stable zinc-ion batteries. *ACS. Energy. Lett.* **2020**, *5*, 3012-20. DOI
37. Zhang, Q.; Ma, Y.; Lu, Y.; et al. Modulating electrolyte structure for ultralow temperature aqueous zinc batteries. *Nat. Commun.* **2020**, *11*, 4463. DOI PubMed PMC
38. Geng, L.; Meng, J.; Wang, X.; et al. Organic-solvent-free primary solvation shell for low-temperature aqueous zinc batteries. *Chem* **2025**, *11*, 102302. DOI
39. Gamsey, S.; Miller, A.; Olmstead, M. M.; et al. Boronic acid-based bipyridinium salts as tunable receptors for monosaccharides and α-hydroxycarboxylates. *J. Am. Chem. Soc.* **2007**, *129*, 1278-86. DOI
40. Xie, F.; Li, H.; Wang, X.; et al. Mechanism for zincophilic sites on zinc-metal anode hosts in aqueous batteries. *Adv. Energy. Mater.* **2021**, *11*, 2003419. DOI

41. Kumari, N.; Chhabra, T.; Kumar, S.; Krishnan, V. Nanoarchitectonics of sulfonated biochar from pine needles as catalyst for conversion of biomass derived chemicals to value added products. *Catal. Commun.* **2022**, *168*, 106467. DOI
42. Cao, F.; Wang, T.; Ji, X. Enhanced visible photocatalytic activity of tree-like ZnO/CuO nanostructure on Cu foam. *Appl. Surf. Sci.* **2019**, *471*, 417-24. DOI
43. Zhang, J.; Jiang, G.; Xu, P.; et al. An all-aqueous redox flow battery with unprecedented energy density. *Energy. Environ. Sci.* **2018**, *11*, 2010-5. DOI
44. Weng, G. M.; Li, Z.; Cong, G.; Zhou, Y.; Lu, Y. C. Unlocking the capacity of iodide for high-energy-density zinc/polyiodide and lithium/polyiodide redox flow batteries. *Energy. Environ. Sci.* **2017**, *10*, 735-41. DOI
45. Xie, C.; Li, T.; Deng, C.; Song, Y.; Zhang, H.; Li, X. A highly reversible neutral zinc/manganese battery for stationary energy storage. *Energy. Environ. Sci.* **2020**, *13*, 135-43. DOI
46. Jin, S.; Shao, Y.; Gao, X.; et al. Designing interphases for practical aqueous zinc flow batteries with high power density and high areal capacity. *Sci. Adv.* **2022**, *8*, eabq4456. DOI PubMed PMC
47. Luo, J.; Hu, B.; Hu, M.; Wu, W.; Liu, T. L. An energy-dense, powerful, robust bipolar zinc-ferrocene redox-flow battery. *Angew. Chem. Int. Ed.* **2022**, *61*, e202204030. DOI PubMed
48. Yang, M.; Xu, Z.; Xiang, W.; et al. High performance and long cycle life neutral zinc-iron flow batteries enabled by zinc-bromide complexation. *Energy. Storage. Mater.* **2022**, *44*, 433-40. DOI
49. Ling, R.; Zhu, Z.; Peng, K.; et al. Dual-function electrolyte additive design for long life alkaline zinc flow batteries. *Adv. Mater.* **2024**, *36*, e2404834. DOI